Atomic-scale spin sensing with a single-molecule at the apex of a scanning tunneling microscope

B. Verlhac,[1] N. Bachellier,[1] L. Garnier,[1] M. Ormaza,[1]
P. Abufager,[2], R. Robles,[3] M.-L. Bocquet,[4] M. Ternes,[5,6*]
N. Lorente,[3,7*] L. Limot,[1*]

[1]Université de Strasbourg, CNRS, IPCMS, UMR 7504, F-67000 Strasbourg, France
[2]Instituto de Física de Rosario, CONICET and Universidad Nacional de Rosario,
Av. Pellegrini 250 (2000) Rosario, Argentina
[3]Centro de Física de Materiales CFM/MPC (CSIC-UPV/EHU),
20018 Donostia-San Sebastián, Spain.
[4]PASTEUR, Département de Chimie, Ecole Normale Supérieure, PSL Research University,
Sorbonne Universités, UPMC Univ. Paris 06, CNRS, 75005 Paris, France
[5]Institute of Physics II B, RWTH Aachen University, 52074 Aachen, Germany
[6]Peter Grünberg Institut (PGI-3), Forschungszentrum Jülich, 52425 Jülich, Germany
[7]Donostia International Physics Center (DIPC), 20018 Donostia-San Sebastián, Spain

*Corresponding author. E-mail: ternes@physik.rwth-aachen.de (M.T.);
nicolas.lorente@ehu.eus (N.L.); limot@ipcms.unistra.fr (L.L.).

[1]

Recent advances in scanning probe techniques rely on the chemical functionalization of the probe-tip termination by a single molecule. The success of this approach opens the prospect of introducing spin sensitivity through the functionalization by a magnetic molecule. We used a nickelocene-terminated tip

[1]This is the author's version of the work. It is posted here by permission of the AAAS for personal use, not for redistribution. The definitive version was published in Science **366** (6465), 623-627 (2019), DOI: 10.1126/science.aax8222 .

(Nc-tip), which offered the possibility of producing spin excitations on the tip apex of a scanning tunneling microscope (STM). When the Nc-tip was 100 picometers away from point contact with a surface-supported object, magnetic effects could be probed through changes in the spin excitation spectrum of nickelocene. We used this detection scheme to simultaneously determine the exchange field and the spin polarization of iron atoms and cobalt films on a copper surface with atomic-scale resolution.

In conventional STM, the magnetic ground state of an isolated atom or molecule is inferred by collecting spin-related fingerprints in the conductance measured with a metallic tip. Isolated atoms or molecules can also serve as spin detectors when controllably moved on the surface with the help of the tip within their local magnetic environment. The magnetic ground state can change in the presence of a magnetic coupling. Exchange and surface-mediated Ruderman-Kittel-Kasuya-Yosida interactions have been spatially mapped in this way by monitoring the zero-bias peak in the differential conductance (dI/dV) associated to the Kondo effect (*1–4*), the tunneling magnetoresistance (*5–7*), the spin excitation spectra and spin relaxation times (*8–11*). Recently, also dipolar and hyperfine interactions have been observed through electrically-driven spin resonances (*12, 13*).

A well-calibrated sensor attached to the tip apex would allow the tip to be freely positioned above a surface target. This detection scheme eliminates surface-mediated interactions and benefits from the vertical-displacement sensitivity of the STM, as the sensor-target distance is no longer imposed by the surface corrugation. Probing a magnetic exchange interaction across a vacuum gap is experimentally demanding (*14–20*) because scanning probe techniques suffer from poor structural and magnetic characterization of the tip apex. To overcome these limitations, we introduce spin sensitivity by functionalizing the tip apex with a single magnetic molecule. Such a strategy has proven successful for collecting chemical and structural

information on surface-supported atoms and molecules otherwise inaccessible with a metallic tip (*21–26*). We used a tip decorated by a spin $S = 1$ nickelocene molecule (Fig. 1A) (*27, 28*), which comprises a Ni atom sandwiched between two C_5H_5 cyclopentadienyl (Cp) rings, and accurately capture the junction geometry through the comparison to first-principles calculations.

We prepared the Nc-tip with atomic control. We first performed soft tip-surface indentations into our pristine working surfaces, either Cu(100) or Cu(111) (*30*), to ensure a monoatomically sharp Cu apex. Nickelocene was then imaged as a ring (inset in Fig. 1B); the molecule adsorbed on copper with one Cp bound to the surface and the other exposed to vacuum (*31*). After transferring the Nc molecule from the surface to the tip —details of the molecule transfer to the tip can be found in (*28*), the Nc-tip was characterized by spectral features found in the second derivative, d^2I/dV^2, of the current I with respect to the bias V measured at a set of constant distances z between tip and the pristine Cu(100) surface (Fig. 1B). We calibrated z by performing controlled tip contacts to the surface tracking the current I and defining $z = 0$ as the distance where the transition from the tunneling to contact regime occurs [see Fig. S1 and accompanying discussion in the supplementary materials (*30*)].

The spectra varied with z only in amplitude and were dominated by a peak at positive and a dip at negative V at energies symmetric to zero. These peaks and dips correspond to inelastic tunneling events in which tunneling electrons excite the Nc from its magnetic ground state $|M = 0\rangle$, with M as the magnetic quantum number projected onto the axis perpendicular to the rings of the molecule, to one of the two degenerate excited states $|M = \pm 1\rangle$. These states are at a higher energy $D = (3.5 \pm 0.1)$ meV relative to the ground state (*27*), where D is the axial magnetic anisotropy [see Eq. (2)]. The inelastic conductance was nearly one order of magnitude greater than the elastic conductance [see Fig. S2 and accompanying discussion in the supplementary materials (*30*)], highlighting that the spin of Nc was well preserved from scattering events with itinerant electrons of the metal (*27, 32*). This response is remarkable,

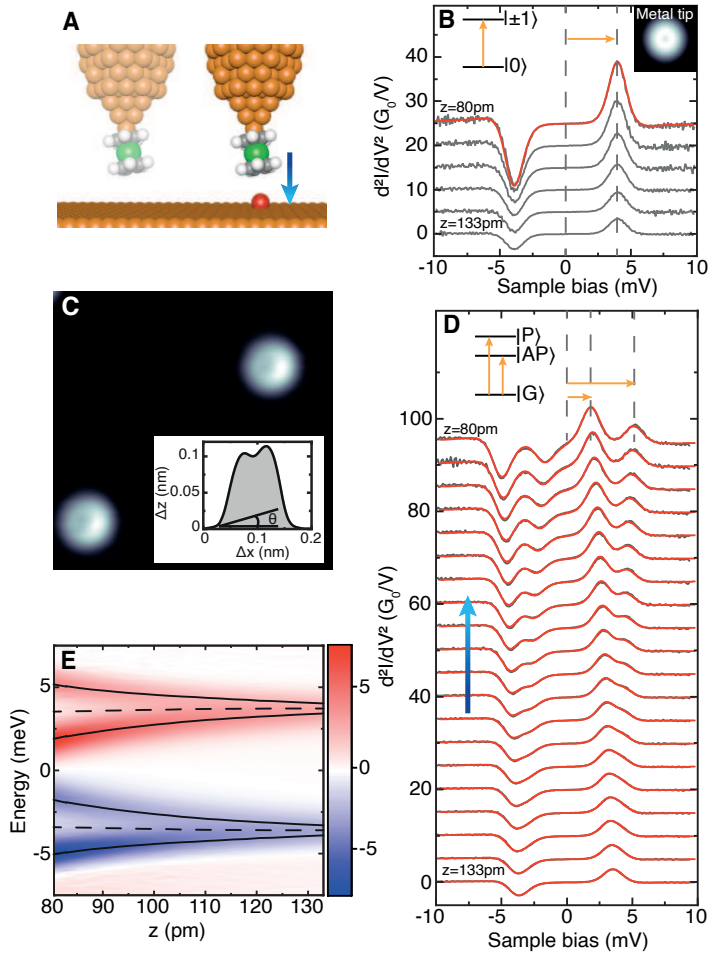

Figure 1: **Spin excitation spectra above the Cu surface and a single Fe atom.** (A) Schematic view of the tunnel junction. Atom colors: Cu (orange), C (gray), H (white), Ni (green), Fe (red). (B) d^2I/dV^2 spectra acquired above a surface atom of Cu(100) at a distance between $z = 133$ and $z = 80$ pm. The solid red line is a fit based on a dynamical scattering model (*29*), and yielded an axial magnetic anisotropy of $D = 3.5$ meV, a coupling between the localized Nc spin and the tip electrons of $J_0\rho_0 = -0.08$, and a spin-conserving potential scattering of $U = 0.02$. Inset: Image of Nc on Cu(100) acquired with a copper-coated tip apex ($V = 20$ mV, $I = 100$ pA, size: 2 nm by 2 nm). (C) Image of Fe atoms on Cu(100) ($V = -15$ mV, $I = 30$ pA, size: 5 nm by 5 nm), and corresponding line profile of one atom (Inset) revealing the presence of a tilted Nc at the tip apex. The tilt angle θ was estimated through the height difference between the left and right protrusion of the line profile. (D) d^2I/dV^2 spectra acquired with the tip positioned above the high-intensity side of the ring-shaped Fe atom. Tip distances $z < 80$ pm resulted in the transfer of Nc atop the Fe atom (Figs. S1B and S1C). (E) Peak and dip energy positions extracted from the spectra of panel (D). The color scale flanking the panel corresponds to the d^2I/dV^2 amplitudes and is given in units of G_0/V. For clarity, the spectra in (B) and (D) were shifted vertically from one another by $5 \times G_0$/V ($G_0 = 2e^2/h$: quantum of conductance).

differentiating Nc from other single atoms or molecules, which instead require a thin insulating spacer between them and the metal surface (*8, 33, 34*) or a superconductor (*35*) to preserve their quantum nature.

We used the Nc-tip to probe surface magnetism through changes in the spin excitation spectrum. We initially probed a single magnetic Fe atom adsorbed on Cu(100) (Fig. 1A). Iron atoms on the surface (*30*) protruded by 115 pm and were imaged with the Nc-tip as rings with an asymmetric apparent height (Fig. 1C). The structure observed in the image reflected the presence of Nc on the tip apex and resulted from the tilted adsorption geometry of the molecule. Indeed, density functional theory (DFT) calculations showed that Nc bonded to the tip-apex atom through two C atoms of the Cp ring (*28*). The tilt angle was estimated through the line profile of the Fe atom (Inset of Fig. 1C), which revealed that the tips used were typically at angles $\lesssim 15^\circ$ relative to the surface normal.

A set of d^2I/dV^2 spectra recorded at different z heights above the Fe atom (Fig. 1D) showed that at $z = 133$ pm, the spectrum was indistinguishable from the one acquired above the bare Cu(100) (Fig. 1B). In this low-energy range, Fe was spectroscopically dark, *i.e.*, its contribution to the spin excitation spectrum was negligible presumably due to strong screening and broadening effects. However, for smaller z heights, we observed a splitting of the peak and the dip that became increasingly stronger as z decreased (Fig. 1E). The average position of the spin-split peaks and dips varied at most by 0.2 meV with distance (dashed line in Fig. 1E).

We tested several Nc-tips with tilt angles ranging from 5° to 15°, and all showed similar behavior —the distances for a given splitting changed only by ± 10 pm. Apart from the splitting, we also observed a striking intensity asymmetry of the split spectral features. Although the amplitudes of the positive peak and negative dip were identical for the Nc-tip probed against the bare surface (Fig. 1B), at positive bias, the energetically lower excitation had higher peak amplitude than the energetically higher excitation, whereas at negative bias the dips showed

opposite behavior compared to the peaks.

The splitting and asymmetry of the line shape observed above Fe have magnetic origin. To rationalize these observations, we assign the z-axis as the out-of-surface direction neglecting the small tilt of the molecule and use a spin Hamiltonian that includes the magnetic anisotropy of the Nc molecule and of the Fe atom on copper (D_{Fe}) (*7, 36*)

$$H = D\hat{S}_z^2 + D_{\mathrm{Fe}}\hat{S}_{z,\mathrm{Fe}}^2 - J\hat{S}_z \cdot \hat{S}_{z,\mathrm{Fe}}, \tag{1}$$

where J is an Ising-like exchange coupling restraining the Nc-Fe magnetic interaction along the z-axis [see Fig. S3 and accompanying discussion in the supplementary materials (*30*)]. Within this framework, the ground state of the combined system is a doublet $|\mathrm{G}\rangle = |0, \Uparrow\rangle$ and $|0, \Downarrow\rangle$ where the energetically lowest states of the Fe spin are noted $\Uparrow$ and $\Downarrow$. The exchange interaction lifts the degeneracy between the two excited doublets $|\mathrm{AP}\rangle$ and $|\mathrm{P}\rangle$ of the coupled spin system and causes the line shape to split apart. As the exchange interaction is antiferromagnetic ($J < 0$, see below) and the Fe is spectroscopically dark, the lowest excited state doublet is $|\mathrm{AP}\rangle = |-1, \Uparrow\rangle$ and $|+1, \Downarrow\rangle$ and corresponds to an antiferromagnetic configuration where the Fe spin is anti-aligned with the Nc spin. The higher excited state doublet corresponds to the ferromagnetic configuration, $|\mathrm{P}\rangle = |+1, \Uparrow\rangle$ and $|-1, \Downarrow\rangle$. Note that for this derivation, neither the spin magnitude of the Fe atom nor the sign of D_{Fe} have to be explicitly set as long as the ground state is a doublet.

To simplify the discussion, it is preferable to express the spin Hamiltonian of Eq. (1) with an effective Zeeman term consisting of the gyromagnetic factor (g), the Bohr magnetron (μ_{B}), and the exchange field (B) produced by the Fe atom and acting along the z-axis of the Nc molecule:

$$\hat{H} = D\hat{S}_z^{\,2} - g\mu_{\mathrm{B}}B\hat{S}_z. \tag{2}$$

This expression has the advantage of providing a common framework for describing the spin systems investigated in the present study. Within mean-field theory $B = J\langle S_{\mathrm{Fe}}\rangle / g\mu_{\mathrm{B}}$, where

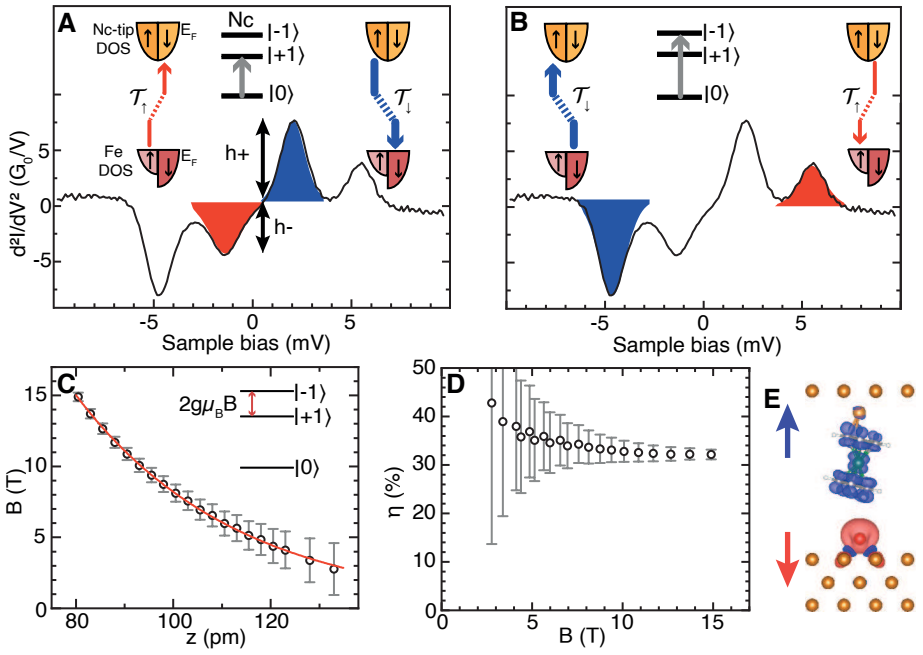

Figure 2: **Inelastic tunneling and magnetic coupling measured above a Fe atom.** (A) and (B) sketch the mechanism leading to the bias asymmetry in the d^2I/dV^2 spectra acquired above Fe. (A) At negative bias, inelastic electrons tunneled from the spin-up states of the Fe atom to the spin-down states of the Nc-tip with transmission proportional to $\mathcal{T}_\uparrow$, leading to a dip in the d^2I/dV^2 spectrum. At positive bias, the junction polarity was reversed and inelastic electrons tunneled from the spin-up states of the Nc-tip to the spin-down states of the Fe atom with transmission proportional to $\mathcal{T}_\downarrow$, leading to a peak in the d^2I/dV^2 spectrum. During the tunneling process, the electrons excited Nc from its ground to its first excited state. The weaker amplitude for the dip compared to the peak reflects the difference in the transmission ($\mathcal{T}_\uparrow \neq \mathcal{T}_\downarrow$). (B) Same mechanism as (A) but for inelastic tunnel electrons exciting Nc from its ground state to its second excited state. (C) Exchange field B and (D) spin-asymmetry η extracted from the spectra of Fig. 1D using Eq. (2). (E) DFT calculated configuration of the tunnel junction for a distance of 100 pm with isosurface of the spin density (antiferromagnetic coupling).

$\langle S_{\mathrm{Fe}} \rangle$ is the effective spin of Fe on the Cu(100) surface. In the following, for clarity we restrain the analysis to a $\Downarrow$ Fe spin, without loss of generality [see Fig. S4 and accompanying discussion in the supplementary materials (*30*)]. The exchange field, within this viewpoint, causes a Zeeman splitting of the line shape into the two excited states $|+1\rangle$ and $|-1\rangle$ of Nc that are located at low and high energy, respectively. The bias asymmetry in the peaks and dips reflects instead a spin imbalance in the tunneling current (*10, 37–39*). This mechanism is sketched in Fig. 2A and 2B. It is qualitatively similar to conventional spin-polarized STM (*5*) and, more generally, to spin valves or to Kondo systems coupled to magnetic electrodes (*4, 18, 40, 41*).

As illustrated in Fig. 2A, the excitation of Nc from the ground state to its first excited state $|+1\rangle$ requires a change in spin angular momentum of $\delta M = +1$. Because the total angular momentum must be conserved, it can only be induced by electrons that compensated for this moment by flipping their spin direction during the tunneling process from $|\uparrow\rangle$ to $|\downarrow\rangle$. At negative bias, the tunneling process may be viewed as a $|\uparrow\rangle$ electron hopping from the substrate into the molecular orbital with transmission $\mathcal{T}_{\uparrow}$, while a $|\downarrow\rangle$ electron is emitted from the molecular orbital toward the Cu tip. At positive bias, the tunneling direction reverses and the transmission from tip to sample is $\mathcal{T}_{\downarrow}$. The relative height of the dip at low negative voltage (h_-) compared to the peak at low positive voltage (h_+) yields a quantitative measure of the spin asymmetry $\eta = (h_+ - h_-)/(h_+ + h_-)$, with $h_- \propto \mathcal{T}_{\uparrow}$ and $h_+ \propto \mathcal{T}_{\downarrow}$. The excitation of Nc from the ground state to its second excited state $|-1\rangle$ requires instead electrons starting in a $|\downarrow\rangle$ state and ending in a $|\uparrow\rangle$ state (Fig. 2B), resulting in a spin asymmetry of $-\eta$.

The spin-polarized nature of the transmission reflects a delicate balance between the spin dependence of the Nc-Fe hybridization and of the density of states (DOS) of both tip and substrate. Neglecting the small tilt angle of Nc relative to the quantization axis z, the Nc-tip DOS is instead unpolarized as the $M = 0$ ground state of Nc leads to a projected moment $\langle m_z \rangle = 0$. As a consequence, the spin polarization of the transmission reflects the polarization of the DOS

of the substrate weighted by the spin-dependent Fe hybridization with the π orbitals of Nc [see Fig. S6 and accompanying discussion in (*30*)].

The fit to the line shape using Eq. (2) and a dynamical scattering model (solid red lines in Fig. 1d) (*10, 29*) was highly satisfactory and provided quantitative values of the spin-asymmetry η and the exchange field B exerted by the Fe atom onto the Nc molecule assuming a gyromagnetic factor of $g = 1.89$ (*42*). The exchange field was an exponential function of z (Fig. 2C), allowing us to exclude a magnetic dipolar interaction. Assuming an exponential decay of the form $\exp -z/\lambda$, we found a decay length $\lambda = (34 \pm 2)$ pm, consistent with other tip-induced exchange interactions (*16, 17, 20, 42*). Different Nc-tips showed similar decay constants [see Fig. S5 in (*30*)]. Using our DFT-computed effective spin of $\langle S_{\mathrm{Fe}} \rangle \approx 1.7$, the exchange coupling was $|J| \approx 0.9$ meV at the shortest probed Fe-Nc distances, typical for a tip-adsorbate exchange interaction across a vacuum gap (*18, 19*). Details regarding the DFT calculations can be found in the supplementary materials (*30*). The magnetic anisotropy D, which corresponds to the average position of the spin-split peaks and dips, remained constant with z (Fig. 1E). This result indicated that the intramolecular structure of Nc was preserved on the tip apex (*27, 43*).

For the data presented in Fig. 1D, we found a spin asymmetry of $\eta = 32\%$ at the highest fields measured (Fig. 2D). The data collected on an ensemble of different Nc-tips on different Fe atoms yielded a lower average value of $\eta = 23\%$ [see Fig. S5 in (*30*)]. The observed spin asymmetry is in agreement with the spin polarization found for electrons inelastically tunneling between a Fe-terminated tip and the quantized states of single adsorbates (*17, 20*).

The sign of the exchange interaction between a magnetic atom and a magnetic tip apex is determined by the competition of direct and indirect interactions and may vary with tip-atom distance (*44*). To gain insight into the exchange coupling between the Nc-tip and Fe atom, we computed with DFT the exchange energy defined as $E_{ex} = E_{\mathrm{P}} - E_{\mathrm{AP}}$ at various Nc-Fe distances by fully relaxing the junction geometry; E_{P} (E_{AP}) is the total energy of the junction with the

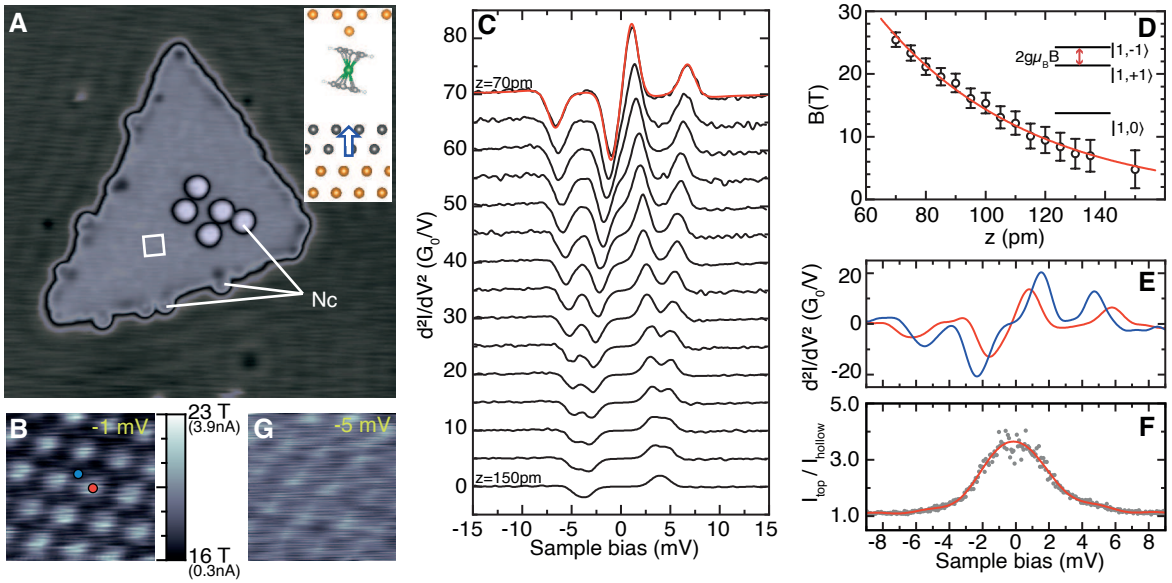

Figure 3: **Spin excitation spectra above a cobalt surface.** (A) Cobalt island on Cu(111) decorated with Nc molecules ($V = -50$ mV, $I = 20$ pA, size: 25 nm by 25 nm). The white lines highlight the presence of Nc. The white square corresponds to the area investigated in (B) and (F). Inset: Schematic view of a Nc-tip above a cobalt island. The arrow indicates the out-of-plane magnetization of the island. (B) Constant-height image acquired in the center of the island at $z = 80$ pm with $V = -1$ mV (size: 1 nm by 1 nm). The color scale indicates the value of the tunnel current and the corresponding B, which is estimated using the exchange coupling of the two spectra in (E). (C) d^2I/dV^2 spectra acquired with the tip positioned above a Co atom of the island. The tip was moved from $z = 150$ pm to $z = 70$ pm. For clarity, the spectra are displaced vertically from one another by 5×10^{-3} G_0/mV. The solid red line is a fit based on a dynamical scattering model. Unlike the fits of Fig. 1D, to correctly capture the line shape we allow the tunneling electrons to produce out-of-equilibrium state populations (*10*) in Nc by solving the dynamical rate equations of the tunneling process (*29*). (D) Exchange field B extracted from the spectra of (C) using Eq. (2). (E) d^2I/dV^2 spectra acquired at $z = 80$ pm above a top site [red dot in (B)] and above a hollow site [blue dot in (B)]. (F) Ratio between the tunnel current above a top site and the tunnel current above a hollow site. (G) Constant-height image of the same area as in (B) also acquired at $z = 80$ pm, but with lower tunnel bias (-5 mV).

spin directions of Nc and Fe in parallel (antiparallel) alignment. To facilitate the comparison to the experimental findings, we took $z = 0$ as the center-to-center distance between the closest carbon atom of Nc and the Fe atom, which is ~ 250 pm. The exchange interaction favored an antiparallel alignment of the two spins (Fig. 2E)—the junction geometry remained constant up to 50 pm, at which distance a chemical bond started to form between Fe and Nc [Fig. S1 in (*30*)]. The energy difference between antiparallel and parallel alignment is 13 meV at 120 pm, while no difference could be evidenced above 300 pm. The antiferromagnetic coupling was short ranged and attributed to the direct hybridization of the Fe orbitals with the frontier molecular orbitals of Nc.

We extended the proof-of-concept for the Nc-tip to a collection of atoms by investigating a prototypical ferromagnetic surface consisting of a nanoscale Co island grown on Cu(111) (Fig. 3A) (*45–48*). The islands are triangular-like and two-layers high with typical lateral extensions ≥ 10 nm for the Co coverage used (*30*). They possess at low temperature an out-of-plane magnetization perpendicular to the Cu surface (Inset of Fig. 3A) (*46, 49, 50*). Unlike the Fe atom, the Co spin is fixed and we assume it to be $\Uparrow$ without loss of generality. We found that Nc adsorbed preferentially on Co, either on top of the nanoislands or on the bottom edge of the island as remarked for other molecules (*51*). Nc-tips were routinely prepared by transferring a molecule from the edge of the island to the Cu-tip apex. Given the low molecular coverage, large pristine areas of Co could be found on the sample.

In Fig. 3B, we present a typical constant-height image acquired in a small area located in the center of a Co island (white square in Fig. 3A) at a bias $V = -1$ mV, which is very close to the Fermi energy. The Co atoms of the island can be readily visualized with the Nc-tip, whereas this resolution is lost above non-magnetic Cu(111) [see Fig. S7A in (*30*)]. This difference points to the magnetic origin of the contrast. At $z = 150$ pm above the Co surface, the spin excitation spectrum (Fig. 3C) was similar to the spectra of Fig. 1B, which indicated that the island was

spectroscopically dark. However, upon vertically approaching a Co atom in the cobalt island, the peak and dip in the d^2I/dV^2 spectrum progressively split apart. Using the spin Hamiltonian of Eq. (2) and $g = 1.89$, we found that the exchange field varied exponentially and reached values as high as 26 T at the shortest distances explored ($z = 70$ pm, Fig. 3D). The decay length was $\lambda = (50 \pm 5)$ pm. Consistent with the exponential decay of the exchange field, we found that the image corrugation increased when decreasing z [see Fig. S7B in (*30*)].

The exchange field originates mostly by direct orbital overlap and corresponds to an exchange coupling of $|J| \approx 3.2$ meV taking our DFT-computed value of $\langle S_{\mathrm{Co}} \rangle \approx 0.9$ for the effective spin of a Co atom. The spectra showed weak spin asymmetry ($\eta = 5\% - 15\%$) and changed in sign at the island rim [see Fig. S8 in (*30*)] in agreement with spin-polarized STM measurements (*46, 47, 50–52*). The spin polarization found is lower compared to STM measurements carried out with a superconducting tip (*53*), hinting to a π orbital influence on the transmission $\mathcal{T}$ as evidenced in other molecular tips (*54, 55*).

To clarify the observed atomic resolution in the constant-height images taken at bias voltages near the Fermi energy, we compare in Fig. 3E two spectra, one with the Nc-tip positioned above a Co atom (designated hereafter as a top site of the surface; red dot in Fig. 3B) and the other with the Nc-tip above a hollow site of the surface (blue dot in Fig. 3B). As shown, the exchange field varied among the two sites and with it the position of the low-energy excitation peak and dip. These moved toward zero bias when the exchange field increased, shifting instead toward $e|V| = D$ when the exchange field decreased.

The shift of the low-energy peak (dip) translated into a variation of the tunneling current I by working at biases sufficiently low. In particular, at $|V| = 1$ mV and $z = 80$ pm, inelastic excitation to the first excited state was possible only when the Nc-tip was placed above the top site; above the hollow site, this channel was closed. The ratio of $I_{\mathrm{top}}/I_{\mathrm{hollow}} \approx 3$ (Fig. 3F) produced a contrast in the constant-height image. At increased absolute bias ($|V| > 5$ mV),

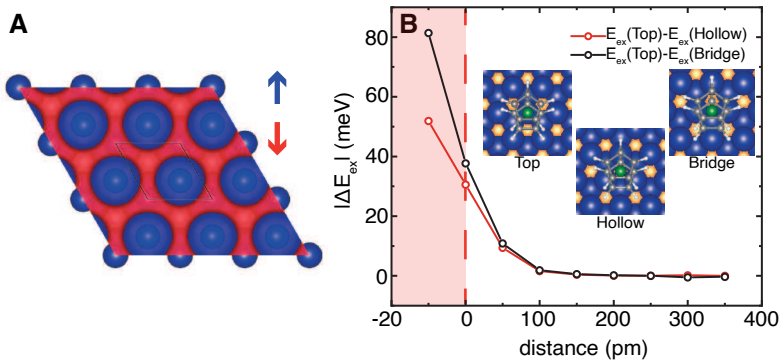

Figure 4: **Computed exchange interaction between Nc and Co.** (A) Isosurface of the spin density for a Co bilayer. Spin-down ($\downarrow$) and spin-up ($\uparrow$) densities are plotted in red (-0.003 Å^{-3}) and blue ($+0.003$ Å^{-3}), respectively. The unit cell is indicated by a black line. Spin-up d electrons are mainly located on the Co atoms, while spin-down sp electrons are dispersive in nature (*45, 47, 50*). The Co atoms had a magnetic moment of 1.76 μ_{B}, which was mainly carried by the d orbitals (d: 1.81 μ_{B}, p: -0.04 μ_{B}, s: -0.01 μ_{B}). The spatial confinement of sp electrons within the island (*45, 47, 50*) was not accounted for. (B) Difference in exchange energy ($|\Delta E_{ex}|$) between the top and the hollow positions (red), and between the top and bridge positions (black). The energy difference was computed as a function of tip distance to the Co surface. The filled red area indicates the contact regime where the Nc molecule is covalently bond to the surface. Inset: Junction geometry used in the DFT calculations defining the top, hollow, and bridge site. Experimentally, the difference in exchange energy between the top and hollow sites is 2 meV when $z = 80$ pm (see peak/dip splittings in Fig. 3E).

$I_{\text{top}}/I_{\text{hollow}}$ was reduced to 1.25, which led to a loss of contrast in the constant-height image (Fig. 3G). To first approximation, the low-bias image shown in Fig. 3B reflected the spatial dependence of the exchange field at the atomic scale [for completeness, Figs. S7C and S7D in (*30*) present a low-bias constant-current image]. Alternatively, it could also be possible to plot the exchange field from the spectra as a function of position, at the expense of considerably increasing the acquisition time of the image.

To confirm the magnetic origin of the contrast, we computed with DFT the exchange energy $E_{ex} = E_{\text{P}} - E_{\text{AP}}$ by varying the distance between the Nc-tip and the Co surface (Fig. 4A). Three locations were investigated, corresponding to a Nc-tip laterally positioned above the surface with its Ni atom centered above a top, hollow, or bridge site of the surface (Inset of Fig. 4B). Just prior to the contact formation between Nc and the surface, which is the distance interval explored in the experiment, the exchange energy was markedly different between these sites (Fig. 4B), because the local character of the d-electrons starts imprinting a lateral corrugation to the interaction. The exchange field can then be expected to change when moving the Nc-tip above the surface, in qualitative agreement with our experimental findings of Fig. 3B. We stress that for a quantitative comparison, which is beyond the scope of the present study, the non-collinearity among magnetic moments of Co and Nc should be taken into account.

The spin excitation spectrum of a Nc molecule attached to the apex of a STM tip can be used to probe the magnetism of an adsorbate and of a surface with atomic-scale resolution. Magnetic information is gathered through the simultaneous measurement of the exchange field across the vacuum gap, as in pioneering magnetic exchange force microscopy experiments (*14, 56*), and of the sample spin polarization at the Fermi level. Unlike conventional spin-polarized STM, the sample spin polarization is determined with minimal influence of the probe on the system owing to the well-characterized Nc-tip apex. A large variety of magnetic systems can be investigated, ranging from systems having resolvable magnetic quantum states (*27, 42*), to systems having a

magnetic moment but non-resolvable quantum states (as shown here). The latter could include single atoms and organometallic molecules on magnetic surfaces, or surfaces with complex magnetic structures. The visualization of complex spin textures should benefit from an external magnetic field, making it possible to experimentally determine the sign of the magnetic exchange interaction (*19, 42*). A minor drawback of the technique is the presence of a tip-related molecular pattern in the images that may however be corrected given a knowledge of the tip status and the possible back-action exerted by the Nc-tip on the sample.

References and Notes

1. A. F. Otte, *et al.*, *Phys. Rev. Lett.* **103**, 107203 (2009).

2. N. Tsukahara, *et al.*, *Phys. Rev. Lett.* **106**, 187201 (2011).

3. N. Néel, *et al.*, *Phys. Rev. Lett.* **107**, 106804 (2011).

4. Y.-S. Fu, Q.-K. Xue, R. Wiesendanger, *Phys. Rev. Lett.* **108**, 087203 (2012).

5. F. Meier, L. Zhou, J. Wiebe, R. Wiesendanger, *Science* **320**, 82 (2008).

6. A. A. Khajetoorians, J. Wiebe, B. Chilian, R. Wiesendanger, *Science* **332**, 1062 (2011).

7. A. A. Khajetoorians, *et al.*, *Phys. Rev. Lett.* **106**, 037205 (2011).

8. C. F. Hirjibehedin, C. P. Lutz, A. J. Heinrich, *Science* **312**, 1021 (2006).

9. X. Chen, *et al.*, *Phys. Rev. Lett.* **101**, 197208 (2008).

10. S. Loth, *et al.*, *Nat. Phys.* **6**, 340 (2010).

11. S. Yan, *et al.*, *Science Adv.* **3** (2017).

12. F. D. Natterer, *et al.*, *Nature* **543**, 226 (2017).

13. P. Willke, *et al.*, *Science* **362**, 336 (2018).

14. U. Kaiser, A. Schwarz, R. Wiesendanger, *Nature* **446**, 522 (2007).

15. J. Bork, *et al.*, *Nat. Phys.* **7**, 901 (2011).

16. R. Schmidt, *et al.*, *Phys. Rev. Lett.* **106**, 257202 (2011).

17. S. Yan, D.-J. Choi, J. A. J. Burgess, S. Rolf-Pissarczyk, S. Loth, *Nat. Nanotechnol.* **10**, 40 (2014).

18. D.-J. Choi, *et al.*, *Nano Lett.* **16**, 6298 (2016).

19. M. Muenks, P. Jacobson, M. Ternes, K. Kern, *Nat. Commun.* **8**, 14119 (2017).

20. K. Yang, *et al.*, *Phys. Rev. Lett.* **122**, 227203 (2019).

21. L. Gross, F. Mohn, N. Moll, P. Liljeroth, G. Meyer, *Science* **325**, 1110 (2009).

22. C. Weiss, *et al.*, *Phys. Rev. Lett.* **105**, 086103 (2010).

23. C.-l. Chiang, C. Xu, Z. Han, W. Ho, *Science* **344**, 885 (2014).

24. C. Wagner, *et al.*, *Phys. Rev. Lett.* **115**, 026101 (2015).

25. J. Guo, *et al.*, *Science* **352**, 321 (2016).

26. H. Mönig, *et al.*, *Nat. Nanotechnol.* **13**, 371 (2018).

27. M. Ormaza, *et al.*, *Nano Lett.* **17**, 1877 (2017).

28. M. Ormaza, *et al.*, *Nat. Commun.* **8**, 1974 (2017).

29. M. Ternes, *New J. Phys.* **17**, 063016 (2015).

30. See supplementary materials for more details.

31. N. Bachellier, *et al.*, *Phys. Rev. B* **93**, 195403 (2016).

32. C. Rubio-Verdú, *et al.*, *Commun. Phys.* **1**, 15 (2018).

33. A. J. Heinrich, J. A. Gupta, C. P. Lutz, D. M. Eigler, *Science* **306**, 466 (2004).

34. I. G. Rau, *et al.*, *Science* **344**, 988 (2014).

35. B. W. Heinrich, L. Braun, J. I. Pascual, K. J. Franke, *Nat. Phys.* **9**, 765 (2013).

36. G. E. Pacchioni, *et al.*, *Phys. Rev. B* **91**, 235426 (2015).

37. T. Balashov, A. F. Takács, W. Wulfhekel, J. Kirschner, *Phys. Rev. Lett.* **97**, 187201 (2006).

38. F. Delgado, J. J. Palacios, J. Fernández-Rossier, *Phys. Rev. Lett.* **104**, 026601 (2010).

39. F. D. Novaes, N. Lorente, J.-P. Gauyacq, *Phys. Rev. B* **82**, 155401 (2010).

40. A. N. Pasupathy, *et al.*, *Science* **306**, 86 (2004).

41. K. von Bergmann, M. Ternes, S. Loth, C. P. Lutz, A. J. Heinrich, *Phys. Rev. Lett.* **114**, 076601 (2015).

42. G. Czap, *et al.*, *Science* **364**, 670 (2019).

43. B. W. Heinrich, L. Braun, J. I. Pascual, K. J. Franke, *Nano Lett.* **15**, 4024 (2015).

44. K. Tao, *et al.*, *Phys. Rev. Lett.* **103**, 057202 (2009).

45. L. Diekhöner, *et al.*, *Phys. Rev. Lett.* **90**, 236801 (2003).

46. O. Pietzsch, A. Kubetzka, M. Bode, R. Wiesendanger, *Phys. Rev. Lett.* **92**, 057202 (2004).

47. O. Pietzsch, *et al.*, *Phys. Rev. Lett.* **96**, 237203 (2006).

48. M. V. Rastei, *et al.*, *Phys. Rev. Lett.* **99**, 246102 (2007).

49. F. Huang, M. T. Kief, G. J. Mankey, R. F. Willis, *Phys. Rev. B* **49**, 3962 (1994).

50. H. Oka, *et al.*, *Science* **327**, 843 (2010).

51. C. Iacovita, *et al.*, *Phys. Rev. Lett.* **101**, 116602 (2008).

52. S. Schmaus, *et al.*, *Nat. Nanotechnol.* **6**, 185 (2011).

53. M. Eltschka, *et al.*, *Nano Lett.* **14**, 7171 (2014).

54. L. Gross, *et al.*, *Phys. Rev. Lett.* **107**, 086101 (2011).

55. B. W. Heinrich, *et al.*, *Phys. Rev. Lett.* **107**, 246801 (2011).

56. J. Grenz, A. Köhler, A. Schwarz, R. Wiesendanger, *Phys. Rev. Lett.* **119**, 047205 (2017).

Acknowledgments

Funding: L.L. acknowledges support by the Agence Nationale de la Recherche (Grant No. ANR-13-BS10-0016, ANR-15-CE09-0017, ANR-11-LABX-0058 NIE, ANR-10-LABX-0026 CSC). M.T. acknowledges support by the Heisenberg Program (Grant No. TE 833/2-1) of the German Research Foundation. N.L. acknowledges support by the Spanish MICINN (Grant No. RTI2018-097895-B-C44). N.L. and R.R. acknowledge support by the EU H2020 FET open project MeMo (Grant No. 766864). **Author contributions:** Experiments were carried out by B.V., N.B., L.G., M.O., and L.L., and calculations were performed by P.A., R.R., M.-L.B., M.T., and N.L. **Competing interests:** The authors declare that they have no competing financial

interests. **Data and materials availability:** All the data are available in the main text and the supplementary materials.

Supplementary materials

Materials and Methods

Supplementary Text

Figs. S1 to S8

References *(57-67)*

Supplementary Materials for "Atomic-scale spin sensing with a single-molecule at the apex of a scanning tunneling microscope"

B. Verlhac,[1] N. Bachellier,[1] L. Garnier,[1] M. Ormaza,[1]
P. Abufager,[2], R. Robles,[3] M.-L. Bocquet,[4] M. Ternes,[5,6*]
N. Lorente,[3,7*] L. Limot,[1*]

[1]Université de Strasbourg, CNRS, IPCMS, UMR 7504, F-67000 Strasbourg, France
[2]Instituto de Física de Rosario, CONICET and Universidad Nacional de Rosario,
Av. Pellegrini 250 (2000) Rosario, Argentina
[3]Centro de Física de Materiales CFM/MPC (CSIC-UPV/EHU),
20018 Donostia-San Sebastián, Spain.
[4]PASTEUR, Département de Chimie, Ecole Normale Supérieure, PSL Research University,
Sorbonne Universités, UPMC Univ. Paris 06, CNRS, 75005 Paris, France
[5]Institute of Physics II B, RWTH Aachen University, 52074 Aachen, Germany
[6]Peter Grünberg Institut (PGI-3), Forschungszentrum Jülich, 52425 Jülich, Germany
[7]Donostia International Physics Center (DIPC), 20018 Donostia-San Sebastián, Spain

*Corresponding author. E-mail: ternes@physik.rwth-aachen.de (M.T.);
nicolas.lorente@ehu.eus (N.L.); limot@ipcms.unistra.fr (L.L.).

Materials and Methods

Experimental methods

The measurements were performed in an ultra-high vacuum STM operating at $T = 2.4$ K. The Cu(100) and Cu(111) surfaces were cleaned *in vacuo* by sputter/anneal cycles, while a sputter-cleaned etched W tip was employed for tunneling. All dI/dV versus bias (V) spectra were

recorded via a lock-in amplifier (modulation: 200 μV rms, frequency: 712 Hz). The d^2I/dV^2 spectra were numerically derived.

Fe on Cu(100): i) We first shortly exposed Cu(100) (surface temperature: $T < 100$ K) to a molecular flux of 2.5×10^{-2} monolayer/min to have single nickelocene (Nc) molecules on terraces or on step edges of the surface. ii) We then sublimated single iron atoms from a Fe wire (99.99% purity) onto Cu(100) (surface temperature: $T < 10$ K) through an opening in the cryostat shields.

Cobalt islands on Cu(111): i) We first sublimated about 1 monolayer of Co with an *e*-beam evaporator at 0.75 monolayer/min onto Cu(111) (surface at room temperature). After deposition, the sample was immediately transferred into the STM. ii) We then dosed single Nc molecules onto the sample (surface temperature: $T < 100$ K) by shortly exposing it to a flux of 2.5×10^{-2} monolayer/min.

Computational methods

We have used DFT to study the two experimental systems: i) a Nc molecule adsorbed on a tip as it approaches a single Fe adsorbed on Cu (100), and ii) a single Nc molecule at different distances from a bilayer of Co on Cu(111). Two implementations of DFT were used in these studies: VASP (*57–62*) has been used to explore the adsorption and TRANSIESTA (*63*) has been used to perform transport calculations. The z-axis is chosen along the surface normal.

Nc-tip above a Fe atom. The molecular geometry was optimized using DFT at the spin-polarized generalized gradient approximation (GGA-PBE). Long-range dispersion corrections were treated at the DFT-D2 level (*64*). We used a plane wave basis set with an energy cutoff of 400 eV. The

core electrons were treated using the projected augmented wave (PAW) method. The same slab is used to represent the substrate where the Fe atom is adsorbed, and the tip where the Nc is adsorbed. The slab geometry is with a 6×6 surface unit cell, 5 layers for the surface holding the tip-apex and the molecule, 6 layers for the approaching surface electrode. The k-point sampling was converged at 3×3, although the sampling was 9×9 for the transmission calculations. For these last calculations, the valence-electron wave functions were double and multiple ζ plus polarization (DZP) basis sets for Nc and diffuse orbitals were used to improve the surface electronic description and a single-ζ plus polarization (SZP) basis set for the copper electrodes.

Nc-tip above a Co bilayer on Cu(111). The cobalt island is described by using a cobalt bilayer. This ferromagnetic monodomain is relaxed on 5 layers of Cu representing a (111) surface in a $6 \times 4\sqrt{3}$ unit cell. The two Co and first three Cu layers were relaxed until forces were below 0.01 eV/Å. The Nc-tip was described by a Nc molecule with a 13° tilt with respect to the substrate normal. Unlike the calculation with the Fe atom, we did not include a metallic electrode in the calculations.

In the TRANSIESTA calculations, a mesh cutoff of 500 Ry, GGA-PBE correlation functional and norm-conserving TroullierMartins pseudo-potentials were employed. Concerning the basis set, the cutoff radius (r_c in Bohr units) and orbitals are $r_c = 3.430$ ($3d$) and $r_c = 6.096$ ($4s$, $4p$) for the Cu electrodes. Diffuse functions were also included to describe surface electrons. In this case, the r_c values and orbitals are 5.247, 2.953 ($3d$), 5.799, 2.187 ($4s$), 5.516 ($4p$) and 7.083 ($5s$). For Fe, $r_c = 8.100$, 5.037, 3.293 ($3d$), $r_c = 8.100$, 7.609, 6.715 ($4s$), and $r_c = 6.001$, 5.853 ($4p$) (*65*). For C, $r_c = 5.383$, 2.881 ($2s$), $r_c = 5.659$ ($2p$), $r_c = 3.029$ ($2d$). For H, $r_c = 6.047$ ($1s$) and $r_c = 1.866$ ($1p$). In the case of Ni, $r_c = 6.474$, 4.340 ($3d$), 6.638 ($4s$), 4.128 ($4p$).

Supplementary Text

Nc-tip: Distance to the surface and dI/dV spectrum

To determine the absolute distance to the surface we controllably bring the Nc-tip into contact with a copper atom of the Cu(111) or Cu(100) surface as in a previous study we carried out (*28*). Contact formation is monitored by recording changes in the tunneling conductance $G = I/V$ as a function of tip-surface distance z. A typical G-vs-z trace acquired at $V = -15$ mV is presented in Fig. S1A. The contact distance ($z = 0$) is identified trough a change in slope of the trace (*66*). Upon retracting the tip, nickelocene remains attached to the tip apex so that the procedure can be repeated several times if necessary. Above a Fe atom, we subtract the apparent height of iron ($h = 115$ pm at $V = -15$ mV) from the contact distance to obtain the absolute distance $[z(\text{Fe}) = z(\text{Cu}) - h]$.

A direct contact of the Nc-tip to the Fe atom is in fact not possible as nickelocene is abruptly transferred to the iron atom at distances $z \leq 80$ pm. This is shown in the image acquired after such a transfer (Fig. S1B), where it can be seen that a new molecular complex is formed. Based on the line profiles (Inset of Fig. S1B), the Nc molecule is located atop the Fe atom, identifying the new complex as a Fe-nickelocene molecule. A similar complex was also observed for another metallocene in earlier work (*67*). We performed density functional theory (DFT) calculations to estimate the magnetic moment of the complex (Fig. S1c). Using atomic projections of the total magnetic moment, we find that the moments carried by Fe and Ni are 3 μ_B and 1 μ_B, respectively. The cyclopentadienyl ligands carry some of the magnetic moment, roughly 0.6 μ_B, giving a spin moment of 1.6 μ_B to nickelocene. Figure S1C indicates an antiferromagnetic coupling between nickelocene and iron, resulting in magnetic moment of 1.4 μ_B for the complex (effective spin of $\approx 1/2$, no orbital moment).

A typical dI/dV acquired with the Nc-tip above a pristine copper surface and its numer-

ical derivative are presented in Figs. S2A and S2B, respectively. The stepped features in the dI/dV are associated to spin excitations revealing that an axial magnetic anisotropy D separates the magnetic ground state $|M_{\mathrm{Nc}} = 0\rangle$ of nickelocene from two degenerate excited states $|M_{\mathrm{Nc}} = \pm 1\rangle$ (*27*). The line shape is accurately simulated by a dynamical scattering model (solid red line in Figs. S2A and S2B) (*29*) from which we extract $D = (3.5 \pm 0.1)$ meV. The step height corresponds to at least a factor 8 increase compared to the elastic conductance ($|eV| < D$), highlighting that the spin of nickelocene is well preserved from scattering events with itinerant electrons of the metal (*27, 32*).

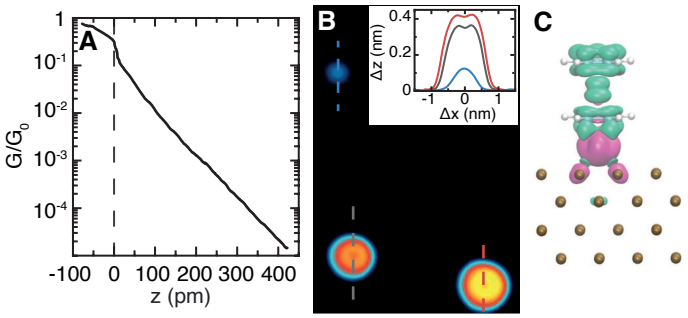

Figure S1: **Conductance versus tip displacement and Fe-nickelocene complex.** (A) G-vs-z trace acquired at a tunnel bias of $V = -15$ mV. The sharp jump to contact reported in (*28*) is smeared out here due to the higher bias employed. (B) Image showing a Fe atom, a nickelocene and a Fe-nickelocene on Cu(100) that was acquired with a metallic tip ($V = -15$ mV, $I = 30$ pA, size: 6×9 nm^2). The corresponding line profiles are shown in the inset (Fe: blue, Nc: dark grey, Fe-Nc: red). (C) DFT computed isosurface of the spin-density of a Fe-nickelocene on Cu(100). The iron atom is adsorbed in a hollow position. Spin-up density: green, spin-down density: magenta.

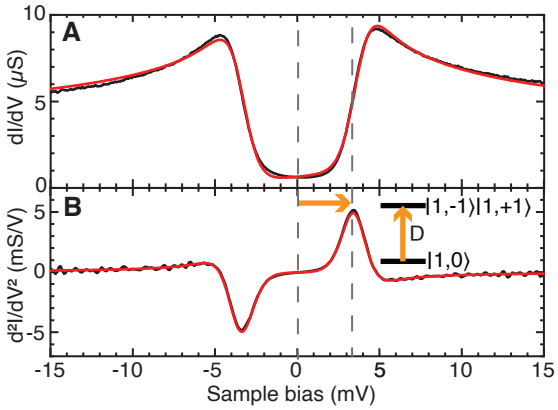

Figure S2: **Spin excitation spectrum of a nickelocene-terminated tip.** (A) dI/dV spectrum and (B) its numerical derivative d^2I/dV^2 acquired with a Nc-tip above Cu(100) (feedback loop opened at -20 mV, 1 nA). The solid red line is a fit based on a dynamical scattering model (*29*), and yields an axial magnetic anisotropy of $D = 3.5$ meV, a coupling between the localized Nc spin and the tip electrons of $J\rho_0 = -0.65$, and a spin-conserving potential scattering of $U = 0.02$.

Model spin Hamiltonian for the Nc-tip above a Fe atom

We model the interaction between the Nc spin-system on the tip with the Fe atom or the Co island on the surface using the simplified Hamiltonian $H = D\hat{S_z}^2 - g\mu_B B\hat{S_z}$ as displayed in Eq. 2 of the main text. This Hamiltonian can be deduced from the following, more general Hamiltonian:

$$H = D_{\mathrm{Nc}}\hat{S}^2_{z,\mathrm{Nc}} + D_{\mathrm{Fe}}\hat{S}^2_{z,\mathrm{Fe}} - \hat{\mathbf{S}}_{\mathrm{Nc}} \cdot \mathbf{J} \cdot \hat{\mathbf{S}}_{\mathrm{Fe}}. \quad (1)$$

Here, the first part of the equation accounts for the known magnetocrystalline anisotropy of the Nc molecule adsorbed on the tip apex. We describe the molecule as an effective spin $S_{\mathrm{Nc}} = 1$, where a $D_{\mathrm{Nc}} > 0$ results in a non-magnetic ground-state with $M = 0$ and two degenerated excited states with $M = \pm 1$. Furthermore, we assign the z-axis as the out-of-surface direction neglecting the small tilt ($< 15°$) of the molecule and the anisotropy axis. The second term accounts for any possible anisotropy of the Fe adatom on Cu(100). Because the Fe atom is spectroscopically "dark", *i.e.* dI/dV spectroscopy does not lead to distinguishable spectroscopic features at the experimental base temperature, we have to derive the spin and possible magnetic anisotropy of the Fe atom on the Cu(100) substrate from other sources. From DFT we find a total magnetic moment of $< m >= 3.4\mu_{\mathrm{B}}$, and extract an effective spin of $S_{\mathrm{Fe}} \approx 3/2$ using $< m >= g\sqrt{S(S+1)}\mu_{\mathrm{B}}$ with $g = 2$. The magnetic moment found is close to the one experimentally determined for a Fe atom adsorbed on Cu(111) (*7, 36*). Because the Fe atom is adsorbed on the hollow site of the highly fourfold symmetric Cu(100) surface and thus belongs to the C_{4v} symmetry, only axial out-of-plane anisotropy for $S_{\mathrm{Fe}} \leq 3/2$ is possible. The sign and strength of D_{Fe} is, however, still unknown. We note that the magnetic anisotropy for Fe on a Cu(111) is $D_{\mathrm{Fe}} = (-0.85 \pm 0.2)$ meV (*7, 36*).

Next, we discuss the last term of the equation, the coupling between the two spin systems. To first order the two spins are coupled via the unknown coupling tensor $\mathbf{J}$. Experimentally,

however, the excitation energies split apart nearly symmetrically relative to their average value (Figs. S3A and S3B; see also Fig. 1e), drastically limiting the coupling possibilities. Because of the out-of-plane quantization axis of the spectroscopically active Nc molecule, only an Ising-like $J_z \hat{S}_{z,\mathrm{Nc}} \cdot \hat{S}_{z,\mathrm{Fe}}$ interaction will result into a symmetric splitting (Fig. S3C). All other couplings, for example Heisenberg-like or in-plane Ising-like couplings will mix the $M = +1$ and $M = -1$ states of the Nc leading to an asymmetric splitting. We note, however, that for $|D_{\mathrm{Fe}}| \gg |J|$ a Heisenberg-like interaction would be indistinguishable from an Ising-like interaction and that the experimental results do not allow to assign if the coupling is ferromagnetic or antiferromagnetic.

Because we do not observe a splitting into three or more peaks/dips when approaching the Fe-atom with the Nc-tip, the absolute value of the magnetic anisotropy D_{Fe} must be larger than $k_{\mathrm{B}}T$ (here 0.2 meV) so that always only one degenerated doublet is significantly occupied. Finally, this enables to simplify the Hamiltonian by neglecting the anisotropy term of the Fe and reformulating the interaction term as $J_z \hat{S}_{z,\mathrm{Fe}} \hat{S}_{z,\mathrm{Nc}} = g\mu_B B \hat{S}_{z,\mathrm{Nc}}$. Figure S4 summarizes the mechanism leading to the bias asymmetry in the d^2I/dV^2 spectrum acquired above Fe. The top panel and bottom panel of Fig. S4 are equivalent. For clarity, only the top panel where the iron spin is pointing downward is presented in the main text (Fig. 2).

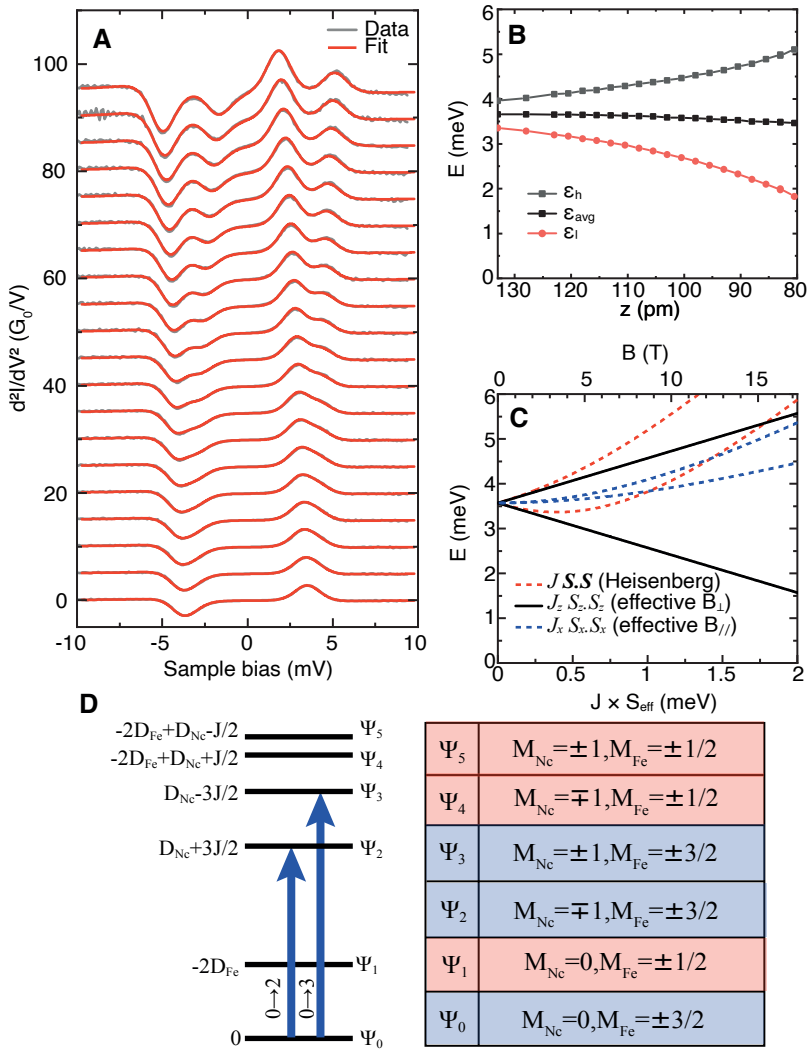

Figure S3: **Spin-spin coupling between Fe and Nc.** (A) Experimental data and simulation as shown in Fig. 1d of the main text. (B) Experimentally determined positions of the two transitions ε_l and ε_h, and their average transition energy ε_{avg}. (C) Simulated development of the transition energies with increasing coupling or exchange field for different coupling scenarios. For simplicity and without loss of generality, we use $S_{\text{Nc}} = 1$ and $S_{\text{Fe}} = 1/2$ (hence $D_{\text{Fe}} = 0$). (D) Spin-state diagram for a nickelocene exchange coupled to the Fe atom with $D_{\text{Fe}} < 0$ and $J < 0$ (antiferromagnetic coupling). We have taken $S_{\text{Nc}} = 1$ and $S_{\text{Fe}} = 3/2$. The eigenfunctions of the system, $|\psi_i\rangle$ $(i = 0, 1, 2, 3, 4, 5)$, are a linear combination of $|M_{\text{Nc}}; M_{\text{Fe}}\rangle$. The blue arrows indicate the spin excitations associated to the nickelocene spectrum. The excitations involving a change in spin momentum for the Fe atom are not detected as iron is "spectroscopically dark" ($\psi_0 \rightarrow \psi_1$ and $\psi_0 \rightarrow \psi_5$) or are forbidden as they do not conserve total spin momentum ($\psi_0 \rightarrow \psi_4$).

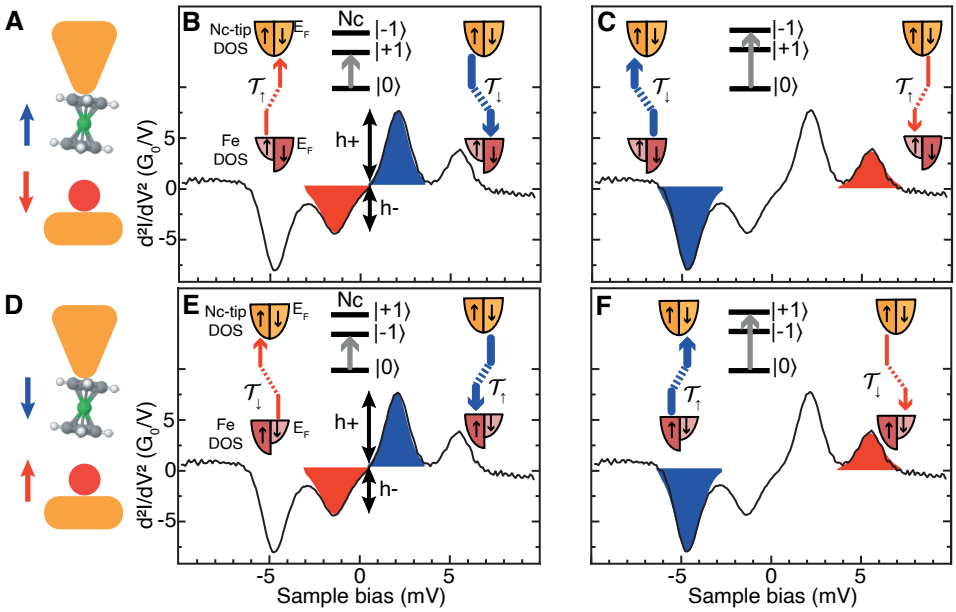

Figure S4: **Inelastic tunneling between a Nc-tip and a Fe atom.** (A) Fe atom with the spin pointing downward ($M_{\mathrm{Fe}} = -3/2$). Panels (B) and (C) sketch the spin-dependent transmission and related spin asymmetry for an anti-parallel ($M_{\mathrm{Nc}} = +1$) and parallel alignment ($M_{\mathrm{Nc}} = -1$) of the Fe and Nc spins, respectively. These correspond to the spin excitations $\psi_0 \rightarrow \psi_2$ and $\psi_0 \rightarrow \psi_3$ in Fig. S3D where $M_{\mathrm{Fe}} = -3/2$. (D) Fe atom with the spin pointing upward ($M_{\mathrm{Fe}} = +3/2$). Panels (E) and (F) sketch the spin-dependent transmission and related spin asymmetry for an anti-parallel ($M_{\mathrm{Nc}} = +1$) and parallel alignment ($M_{\mathrm{Nc}} = -1$) of the Fe and Nc spins, respectively. These correspond to the spin excitations $\psi_0 \rightarrow \psi_2$ and $\psi_0 \rightarrow \psi_3$ in Fig. S3D where $M_{\mathrm{Fe}} = +3/2$.

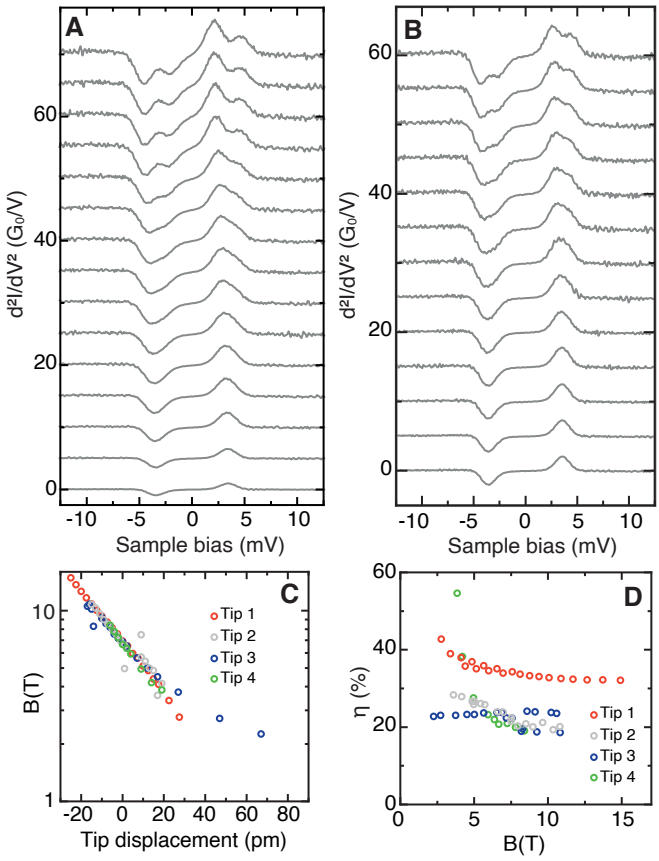

Figure S5: **Inelastic tunneling and tip dependence.** (A) and (B) present d^2I/dV^2 spectra acquired above a Fe atom of Cu(100) using the Nc-tips labeled 2 and 4 in (C) and (D). (C) Exchange field B, and (D) spin-asymmetry η, extracted from the spin excitation spectra acquired above a Fe atom. Four different Nc-tips were used (labeled 1 to 4). Tip 1 corresponds to the tip used to acquire the data of Fig. 1.

Computed elastic transmission: Nc-tip above a Fe atom

We present here the computed spin-dependent elastic transmission (Fig. S6A) for a Nc-tip positioned above a single Fe atom on Cu(100). The calculations are performed for a molecule-Fe distance of 350 pm as measured from the Fe atomic-plane to the closest molecular C-plane, which corresponds approximately to a distance of 100 pm from the contact regime. We consider the magnetic coupling depicted in Fig. 2E where the Fe and Nc spins are collinear and antiferromagnetic, and choose the spin-down direction to be the one fixed by the magnetic moment of the Fe atom. The elastic transmission computed in this collinear configuration is presented in Fig. S6B. Please note that it does not reflect the experimental transmission where the spins are non-collinear, but still provides qualitative information on the orbital contribution to the transmission. The density of states projected on the atomic orbitals (PDOS) of Nc and of Fe are presented in Figs S6C to S6F. The transmission has a strong molecular π character originating in the d_{xz} and d_{yz} orbitals of Ni and the $2p$ orbitals of C as may be concluded form the PDOS of nickelocene. The transmission at the Fermi level is controlled by the empty π orbitals of the molecule and highly polarizes the spin of the transmitted electrons. From Fig. S6B, we obtain the ratio between the elastic transmissions for the two spin channels (spin-up: $T_{\uparrow}$, spin-down: $T_{\downarrow}$). Spin up refers to a spin aligned with the Nc molecular spin, while spin down refers to a spin anti-aligned with the Nc molecular spin, *i.e.* aligned with the Fe spin. We define the spin polarization at the Fermi level for elastic electrons as

$$P = (T_{\uparrow} - T_{\downarrow})/(T_{\uparrow} + T_{\downarrow}), \tag{2}$$

and find $P = -82\%$. This spin polarization is close to the one found for a Nc-tip above a bare Cu(100) where $P = -74\%$ (*28*), confirming that the transmission is mainly governed by the π orbitals of Nc with a minor contribution from the Fe atom.

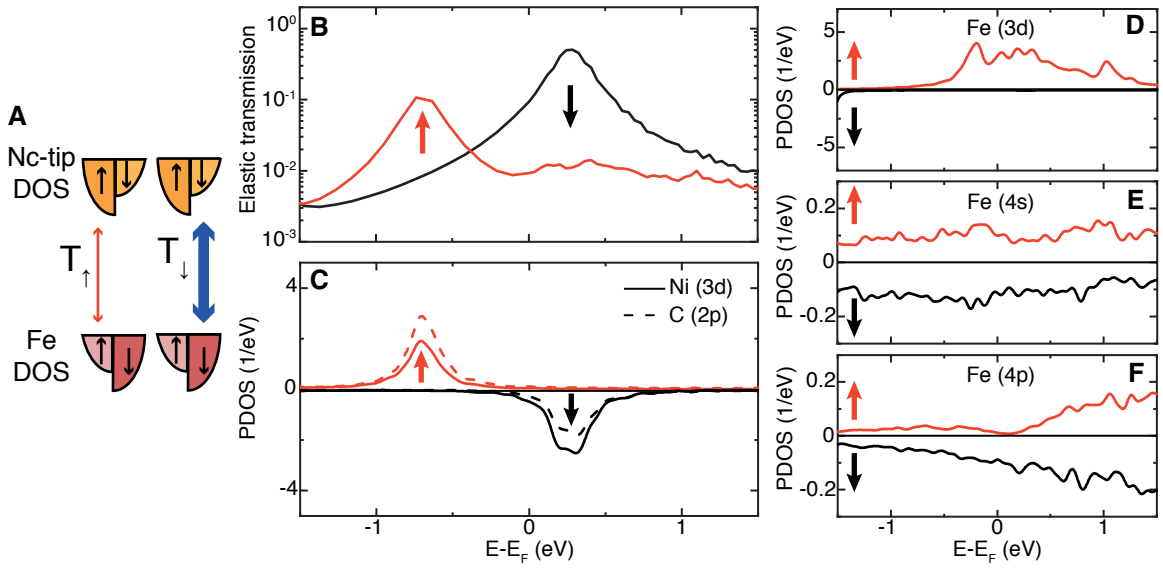

Figure S6: **Computed electronic structure of the Fe-Nc junction.** (A) Schematic representation of the spin-polarized elastic transmissions $T_{\uparrow}$ and $T_{\downarrow}$ between Nc and the Fe atom. (B) Spin-resolved electron transmission as a function of electron energy with respect to the Fermi energy. (C) PDOS on the d-manifold of Ni (solid line) and on the p-orbitals of the C atoms (dashed line) of the Nc molecule. The transmission curves for each spin coincide with the contributions from the PDOS of Ni and C, showing the molecular character of the transmission close to the Fermi energy. (D)-(F) PDOS onto the $3d$, $4s$ and $4p$ atomic orbitals of Fe, respectively. Spin-up structure is in red ($\uparrow$) and spin-down structure is in black ($\downarrow$). The d orbitals of Fe have a strong spin-up contribution at the Fermi level, which is of minority character in view of the direction chosen for the magnetic moment of the Fe atom. The p orbitals have instead a strong spin-down contribution and s orbitals have similar contributions for the two spin-channels.

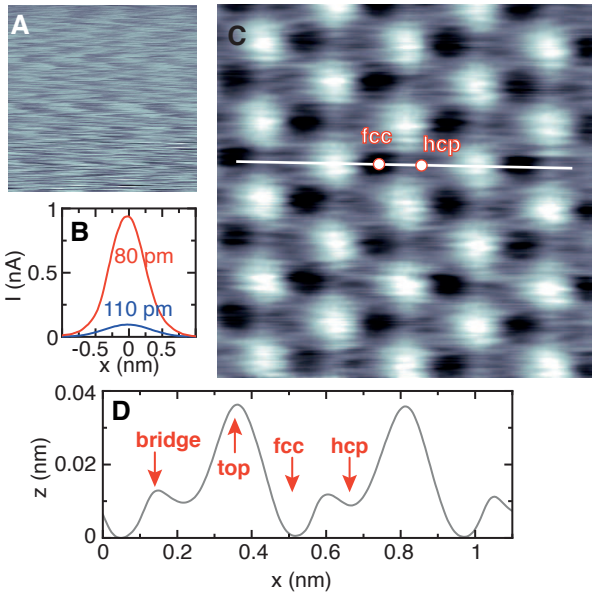

Figure S7: **Magnetic contrast and constant-current imaging.** (A) Constant-height image acquired at $z = +50$ pm above Cu(111) (sample bias: $V = -2$ mV, size: 1 nm by 1 nm). The image is featureless. (B) Line profiles of Co atom extracted from constant-height images of a Co island. The images were acquired at $z = 80$ pm and $z = 110$ pm. (C) Constant-current image acquired in the center of a Co island ($V = -0.5$ mV, $I = 600$ pA, size: 1.2 nm by 1.2 nm) and, (D), corresponding line profile [solid white line in (C)]. A bright contrast in the image indicates a high Nc-Co exchange coupling, while a dim contrast indicates a low Nc-Co exchange coupling. Indeed, when the exchange coupling increases, the low-bias spin excitation of Nc moves toward the Fermi level causing the tunnel current to increase (see Fig. 3E). The tip then retracts to keep the current constant and the corrugation in the image increases. When the exchange coupling decreases, the low-bias excitation moves to lower (higher) energies at negative (positive) bias, causing the image corrugation to decrease. The top sites of the Co surface are readily visualized in the constant-current image. Additionally, some exchange coupling is present on the bridge and hollow sites of the surface. Two distinct hollow sites are resolved, and assigned to the *fcc* and *hcp* sites of the Co bilayer. The strongest coupling is attributed to the *hcp* site and the weakest to the *fcc* site, given the presence of a Co atom below the *hcp* site compared to the *fcc* site. This suggests that constant-current images yield a subsurface resolution of the exchange coupling.

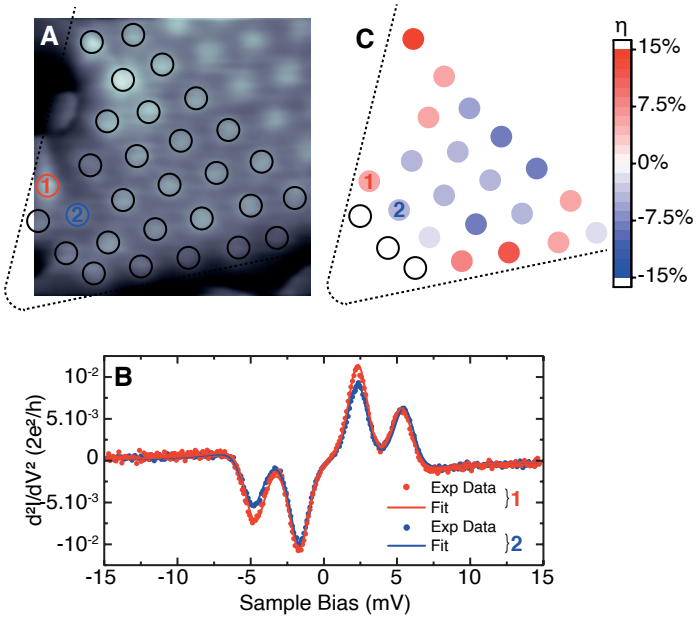

Figure S8: **Imaging the edges of a Co island with a Nc-tip.** (A) Constant-height image acquired at $z = 100$ pm (sample bias: $V = -2$ mV, size: 1.5 nm by 1.5 nm). The image shows an atomic-scale contrast similar to that of Fig. 3B. The top sites are highlighted by black circles; the dashed line highlights the island edges. The Nc-tip used is different from the one of Fig. 3. (B) d^2I/dV^2 spectra acquired above the sites labeled **1** (in red) and **2** (in blue) in (A) at $z = 100$ pm. (C) Spin asymmetry η evaluated from the d^2I/dV^2 spectra acquired above a top site at $z = 100$ pm. The spin asymmetry ranges from -15% to $+15\%$ and changes in sign within one atomic spacing from the island edge. To correctly fit the line shape, we allowed the tunneling electrons to produce out-of-equilibrium state populations (*10*) in Nc by solving the dynamical rate equations of the tunneling process (*29*).

References and Notes

1. A. F. Otte, *et al.*, *Phys. Rev. Lett.* **103**, 107203 (2009).

2. N. Tsukahara, *et al.*, *Phys. Rev. Lett.* **106**, 187201 (2011).

3. N. Néel, *et al.*, *Phys. Rev. Lett.* **107**, 106804 (2011).

4. Y.-S. Fu, Q.-K. Xue, R. Wiesendanger, *Phys. Rev. Lett.* **108**, 087203 (2012).

5. F. Meier, L. Zhou, J. Wiebe, R. Wiesendanger, *Science* **320**, 82 (2008).

6. A. A. Khajetoorians, J. Wiebe, B. Chilian, R. Wiesendanger, *Science* **332**, 1062 (2011).

7. A. A. Khajetoorians, *et al.*, *Phys. Rev. Lett.* **106**, 037205 (2011).

8. C. F. Hirjibehedin, C. P. Lutz, A. J. Heinrich, *Science* **312**, 1021 (2006).

9. X. Chen, *et al.*, *Phys. Rev. Lett.* **101**, 197208 (2008).

10. S. Loth, *et al.*, *Nat. Phys.* **6**, 340 (2010).

11. S. Yan, *et al.*, *Science Adv.* **3** (2017).

12. F. D. Natterer, *et al.*, *Nature* **543**, 226 (2017).

13. P. Willke, *et al.*, *Science* **362**, 336 (2018).

14. U. Kaiser, A. Schwarz, R. Wiesendanger, *Nature* **446**, 522 (2007).

15. J. Bork, *et al.*, *Nat. Phys.* **7**, 901 (2011).

16. R. Schmidt, *et al.*, *Phys. Rev. Lett.* **106**, 257202 (2011).

17. S. Yan, D.-J. Choi, J. A. J. Burgess, S. Rolf-Pissarczyk, S. Loth, *Nat. Nanotechnol.* **10**, 40 (2014).

18. D.-J. Choi, *et al.*, *Nano Lett.* **16**, 6298 (2016).

19. M. Muenks, P. Jacobson, M. Ternes, K. Kern, *Nat. Commun.* **8**, 14119 (2017).

20. K. Yang, *et al.*, *Phys. Rev. Lett.* **122**, 227203 (2019).

21. L. Gross, F. Mohn, N. Moll, P. Liljeroth, G. Meyer, *Science* **325**, 1110 (2009).

22. C. Weiss, *et al.*, *Phys. Rev. Lett.* **105**, 086103 (2010).

23. C.-l. Chiang, C. Xu, Z. Han, W. Ho, *Science* **344**, 885 (2014).

24. C. Wagner, *et al.*, *Phys. Rev. Lett.* **115**, 026101 (2015).

25. J. Guo, *et al.*, *Science* **352**, 321 (2016).

26. H. Mönig, *et al.*, *Nat. Nanotechnol.* **13**, 371 (2018).

27. M. Ormaza, *et al.*, *Nano Lett.* **17**, 1877 (2017).

28. M. Ormaza, *et al.*, *Nat. Commun.* **8**, 1974 (2017).

29. M. Ternes, *New J. Phys.* **17**, 063016 (2015).

30. See supplementary materials for more details.

31. N. Bachellier, *et al.*, *Phys. Rev. B* **93**, 195403 (2016).

32. C. Rubio-Verdú, *et al.*, *Commun. Phys.* **1**, 15 (2018).

33. A. J. Heinrich, J. A. Gupta, C. P. Lutz, D. M. Eigler, *Science* **306**, 466 (2004).

34. I. G. Rau, *et al.*, *Science* **344**, 988 (2014).

35. B. W. Heinrich, L. Braun, J. I. Pascual, K. J. Franke, *Nat. Phys.* **9**, 765 (2013).

36. G. E. Pacchioni, *et al.*, *Phys. Rev. B* **91**, 235426 (2015).

37. T. Balashov, A. F. Takács, W. Wulfhekel, J. Kirschner, *Phys. Rev. Lett.* **97**, 187201 (2006).

38. F. Delgado, J. J. Palacios, J. Fernández-Rossier, *Phys. Rev. Lett.* **104**, 026601 (2010).

39. F. D. Novaes, N. Lorente, J.-P. Gauyacq, *Phys. Rev. B* **82**, 155401 (2010).

40. A. N. Pasupathy, *et al.*, *Science* **306**, 86 (2004).

41. K. von Bergmann, M. Ternes, S. Loth, C. P. Lutz, A. J. Heinrich, *Phys. Rev. Lett.* **114**, 076601 (2015).

42. G. Czap, *et al.*, *Science* **364**, 670 (2019).

43. B. W. Heinrich, L. Braun, J. I. Pascual, K. J. Franke, *Nano Lett.* **15**, 4024 (2015).

44. K. Tao, *et al.*, *Phys. Rev. Lett.* **103**, 057202 (2009).

45. L. Diekhöner, *et al.*, *Phys. Rev. Lett.* **90**, 236801 (2003).

46. O. Pietzsch, A. Kubetzka, M. Bode, R. Wiesendanger, *Phys. Rev. Lett.* **92**, 057202 (2004).

47. O. Pietzsch, *et al.*, *Phys. Rev. Lett.* **96**, 237203 (2006).

48. M. V. Rastei, *et al.*, *Phys. Rev. Lett.* **99**, 246102 (2007).

49. F. Huang, M. T. Kief, G. J. Mankey, R. F. Willis, *Phys. Rev. B* **49**, 3962 (1994).

50. H. Oka, *et al.*, *Science* **327**, 843 (2010).

51. C. Iacovita, *et al.*, *Phys. Rev. Lett.* **101**, 116602 (2008).

52. S. Schmaus, *et al.*, *Nat.e Nanotechnol.* **6**, 185 (2011).

53. M. Eltschka, *et al.*, *Nano Lett.* **14**, 7171 (2014).

54. L. Gross, *et al.*, *Phys. Rev. Lett.* **107**, 086101 (2011).

55. B. W. Heinrich, M. V. Rastei, D.-J. Choi, T. Frederiksen, L. Limot, *Phys. Rev. Lett.* **107**, 246801 (2011).

56. J. Grenz, A. Köhler, A. Schwarz, R. Wiesendanger, *Phys. Rev. Lett.* **119**, 047205 (2017).

57. G. Kresse, J. Hafner, *Phys. Rev. B* **47**, 558 (1993).

58. G. Kresse, J. Hafner, *Phys. Rev. B* **48**, 13115 (1993).

59. G. Kresse, J. Furthmüller, *Comput. Mater. Sci.* **6**, 15 (1996).

60. G. Kresse, J. Furthmüller, *Phys. Rev. B* **54**, 11169 (1996).

61. G. Kresse, D. Joubert, *Phys. Rev. B* **59**, 1758 (1999).

62. J. Hafner, *J. Comput. Chem.* **29**, 2044 (2008).

63. N. Papior, N. Lorente, T. Frederiksen, A. Garca, M. Brandbyge, *Comput. Phys. Commun.* **212**, 8 (2017).

64. S. Grimme, *J. Comput. Chem.* **27**, 1787 (2006).

65. P. Rivero, *et al.*, *Comput. Mater. Sci.* **98**, 372 (2015).

66. L. Limot, J. Kröger, R. Berndt, A. Garcia-Lekue, W. A. Hofer, *Phys. Rev. Lett.* **94**, 126102 (2005).

67. M. Ormaza, *et al.*, *Nano Lett.* **16**, 588 (2016).